Benchmark Calculation of the MEGAPIE Target (M1)

L. Maciocco, V. Moreau, L. Sorrentino
CRS4, Centre for Advanced Studies, Research and Development in Sardinia

S. Buono
CERN, European Organisation for Nuclear Research

February 2002

Abstract

The benchmark calculations performed by CRS4 with Star-CD on a reference geometry of the MEGAPIE target are presented in this report (benchmark M1). Scope of the benchmark is a comparison of the results obtained by the various partners involved in the MEGAPIE project using different codes and turbulence modelling approaches.

The considered target geometry is the one with the final part of the guide tube slanted at an angle of about 9 degrees. The Pb-Bi flow in the last 2150 mm of the target have been simulated, including the calculation of the thermal field in all the solid structures (window, hull and flow guide). Due to geometrical symmetry, only half of the real domain was considered. Turbulence was simulated using a Chen k-ε model, combined with a Two-layer model in the most critical near-wall regions (window and flow guide in the spallation region) and with Wall Functions along the riser and the down-comer. Modified wall functions for low Prandtl number fluids were implemented.

Results are presented for both cases with the beam footprint major axis parallel (benchmark M1.0) and normal (benchmark M1.1) to the guide-tube slant. In order to estimate the effect of the variation of the turbulent Prandtl number on the heat exchange, two calculation have been performed, one with $Pr_t = 0.9$ and one using a relationship $Pr_t = f(Re_t, Pr)$, yielding a locally variable turbulent Prandtl number.

Results show a very complex flow pattern in the spallation region, with 3D vortex structures being generated in the reversing region and dragged along the rising duct.

In case M1.0 with $Pr_t = 0.9$, results show maximum window temperatures of 521 °C and 487 °C in the external and internal side respectively, with a maximum Pb-Bi temperature of 486 °C located nearby the window centre. The maximum flow velocity is 1.35 m/s. A significant heat exchange takes place across the 1.5 mm thick flow guide, causing a mean temperature increase along the down-comer of about 34 °C. Due to the high Reynolds number of the flow, the effect of using a variable Pr_t is limited to near wall regions, where the heat exchange is slightly reduced. The combination of a lower heat exchange across the flow guide (resulting in a lower temperature increase of the Pb-Bi along the down-comer) and a worse window cooling yielded a maximum window temperature of 524°C, namely 3 °C more than in the case with $Pr_t = 0.9$.

In case M1.1, maximum window temperatures of 447 °C and 414 °C were found using $Pr_t = 0.9$ with a maximum Pb-Bi temperature of 423 °C located in the central part of the spallation region. Using a variable Pr_t, window temperatures increased of about 2 °C while a 1 °C lower maximum Pb-Bi temperature was found.

Contents

1 Introduction

In all design activities related to Accelerator Driven Systems [1][2][3], CFD codes are widely used for the design of the cooling circuits of the machine. In particular, for the design of spallation targets, which are the most critical components being subject to very intense heat fluxes, a detailed and extensive fluid-dynamic analysis is compulsory in order to be able to keep temperatures in the target structures within acceptable limits, while keeping flow velocities as low as possible to reduce corrosion problems [4].

Heavy Liquid Metals (HLM) are generally used in ADS spallation targets both as spallation material and cooling fluid [5][6]. This introduces a further uncertainty in the CFD simulation, beyond the standard uncertainty related to CFD simulation in complex geometry, mainly due to the low Pr number of HLM. These problems are being currently studied within the ASCHLIM EU project [7], which involves the greater part of the European ADS community.

In the framework of the MEGAPIE project [8], a benchmarking activity has been set up, including all the partners performing CFD simulations for the design of the MEGAPIE target, in order to be able to estimate the reliability of the results, obtained with different codes and modelling approaches.

Among the various geometry studied for the MEGAPIE target, the one with the slanted guide tube and without bypass flow has been chosen for the benchmarking purpose (benchmark M1) [9][[10]. Two options are considered for the orientation of the proton beam distribution, with the beam footprint major axis aligned with (benchmark M1.0) and perpendicular to (benchmark M1.1) the guide-tube slant.

The results of the simulation of benchmark M1.0 performed by CRS4 with Star-CD are presented in this report.

2 Geometrical Description

The MEGAPIE target (see Figure 1) consists of a steel cylindrical container (hull) closed at the bottom by a hemisphere (window). A steel cylindrical guide tube separates the cold flow down-coming in the external annular channel from the hot flow rising in the central duct. An instrumentation rod is placed in the middle of the riser. The proton beam hits the window from below and the spallation takes place in the flow reversing-zone.

The geometry adopted for the M1 benchmark, illustrated in Figure 1, is a portion of 2150 mm of the MEGAPIE target, which includes part of the central instrumentation rod. In the spallation region, the solution with slanted guide-tube is considered, which makes the geometry non axial-symmetric. However, the geometry is still symmetric with respect to the y-z plane cutting the model in two halves.

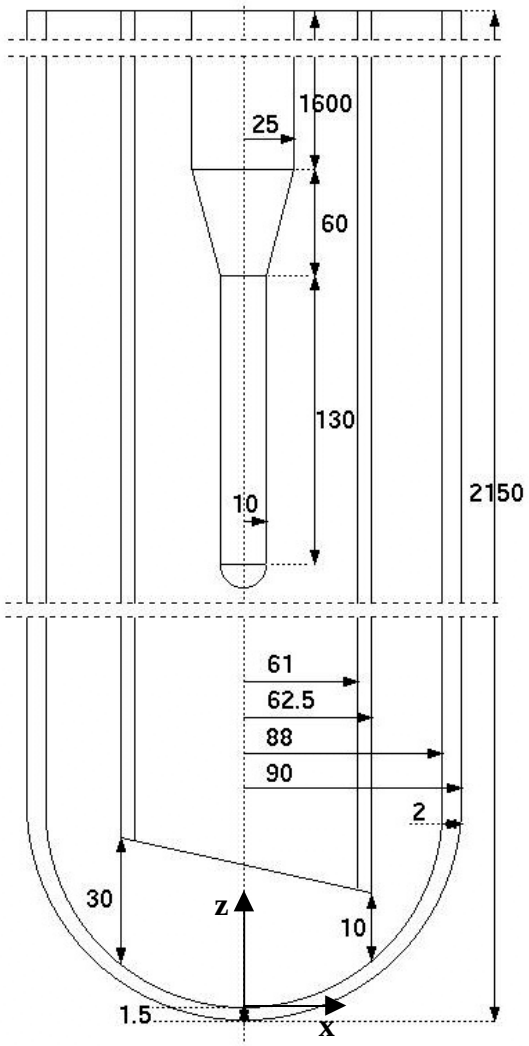

Figure 1 - Description of the MEGAPIE target geometry used for benchmark M1.

3 Physical Description

The test case consists of a lead-bismuth-eutectic flow incoming from the top in the external annulus of the target, flowing downwards towards the steel window, reversing and flowing up towards the outlet section, placed on the top of the central annulus. In the window region, up to a height of about 270 mm, both the fluid and the solid structures are heated by the volumetric heat source generated by the spallation process. The main heat exchanges taking place in the target are the cooling of the window, of the hull and of the lower part of the guide tube, and the heat transfer from the rising flow to the down-coming flow across the guide tube.

The window and the hull are made of T-91 steel and the guide tube is made of AISI-316 steel. The relevant material properties are listed in Table 1. The inlet-flow characteristics are listed in Table 2.

Property	Lead Bismuth Eutectic (T in K)	T91 steel	AISI 316 steel
Density [kg/m^3]	11112.38 - 1.37 T	7800	8000
Thermal conductivity [W/ m K]	3.029214×10^{-5} T^2 - 1.831813×10^{-2} T +11.48094	28.8	18.3
Specific heat [J / kg K]	146.5	562.69	500
Molecular viscosity [Pa s]	4.713675×10^{-9} T^2 - 8.9224×10^{-6} T + 5.371479×10^{-3}	-	-
Prandtl number at 230 ^{o}C	3.06×10^{-2}	-	-

Table 1 - Materials properties.

Mass flow rate	40 Kg/s
Inlet mean velocity	0.323 m/s
Inlet temperature	230 ^{o}C
Inlet Reynolds number	80,000

Table 2 - Inlet flow characteristics

4 Computational Model

The CAD geometry and the computational mesh were built up using the IDEAS software [11]. Star-CD [12] was used to set up the CFD model and to run the simulation.

4.1 Computational domain and mesh

The CAD computational model is illustrated in Figure 2, together with the position of the inlet (in red), outlet (in green) and symmetry (in blue) boundary conditions. Solid structures are actually simulated, apart from the instrumentation rod, solving the thermal diffusion equation with the spallation heat as a source term. Only the part of the external hull within the spallation region was modelled, having considered the target external walls adiabatic. The instrumentation rod was modelled as an adiabatic wall.

A mixed structured-unstructured computational mesh was built, using hexahedral, tetrahedral and prismatic elements. Both integral and arbitrary matching were used to join the various parts of the domain meshed in different ways. A layer of structured hexahedral cells was used in all near-wall regions, with different mesh densities depending on the near-wall turbulence model used (see Section 4.3). The number of fluid cells is about 550,000, with a denser meshing in the spallation region; 36,000 cells were used for the window and the hull and about 20,000 for the guide tube, for a total number of cells of about 600,000.

Details of the mesh are illustrated in Figure 3, Figure 4, Figure 5 and Figure 6.

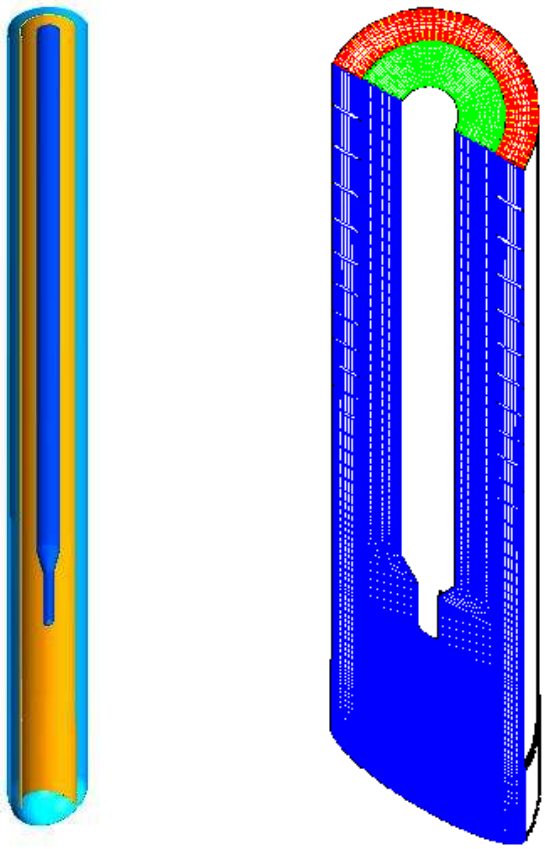

Figure 2 - Computational CAD model (left) and location of boundary conditions (inlet in red, outlet in green and symmetry plane in blu).

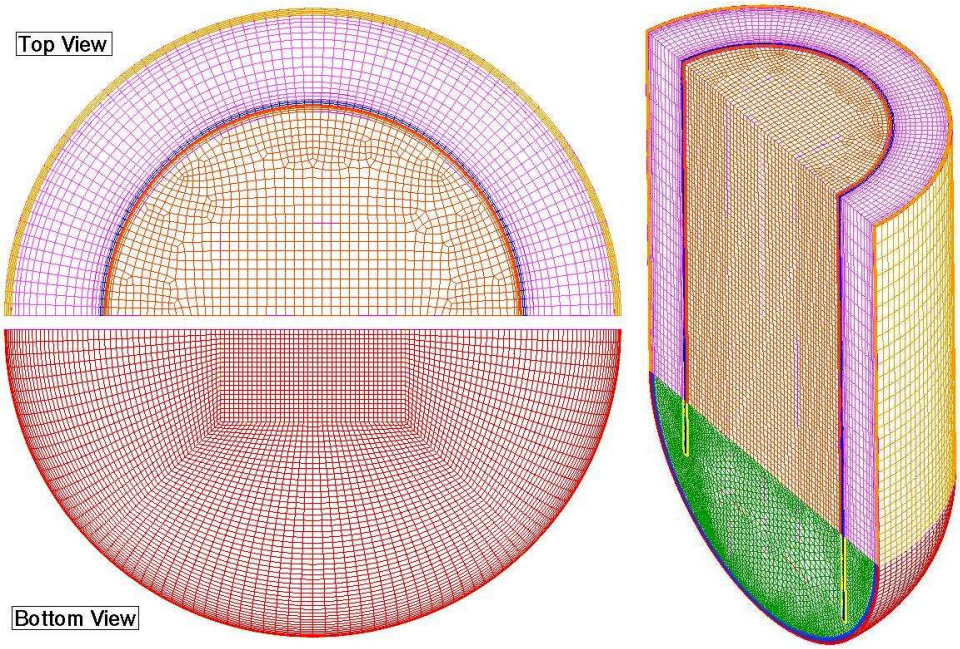

Figure 3 - Computational mesh: top, bottom and isometric views of the lower part.

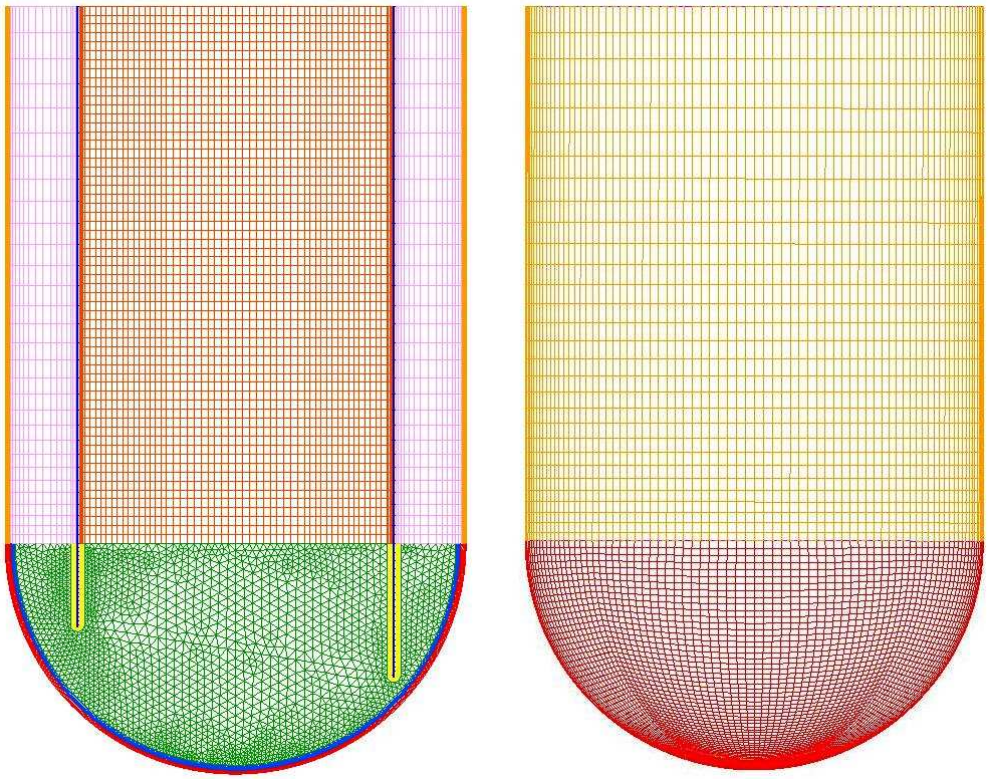

Figure 4 - Computational mesh: front and rear views of the lower part.

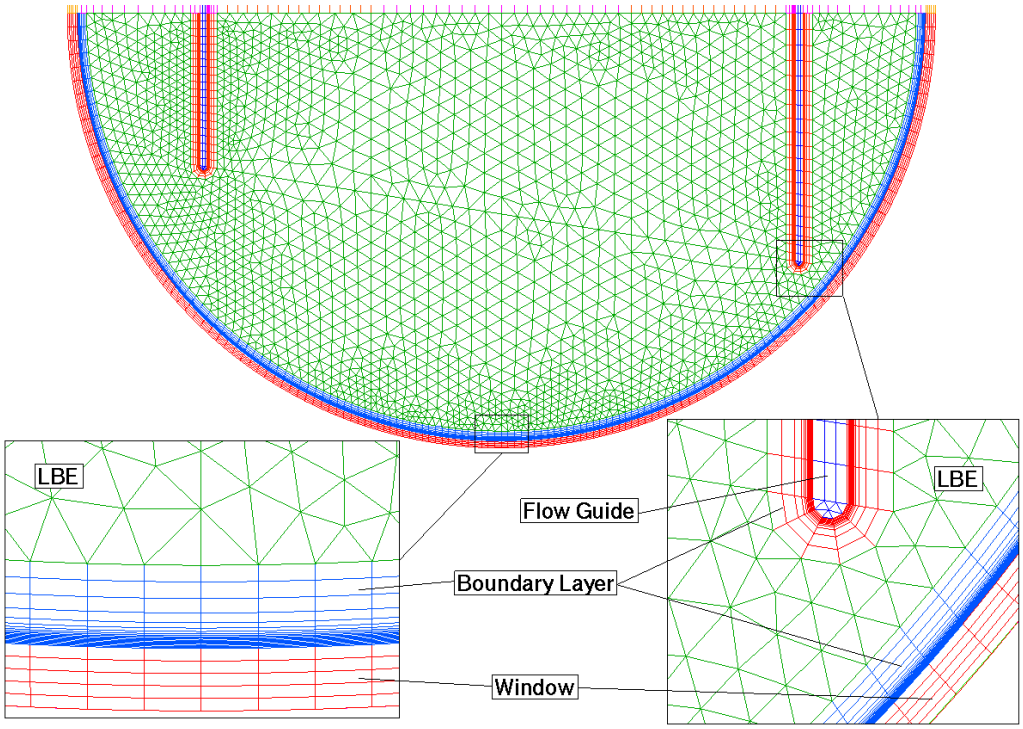

Figure 5 - Computational mesh: details of the near-window region.

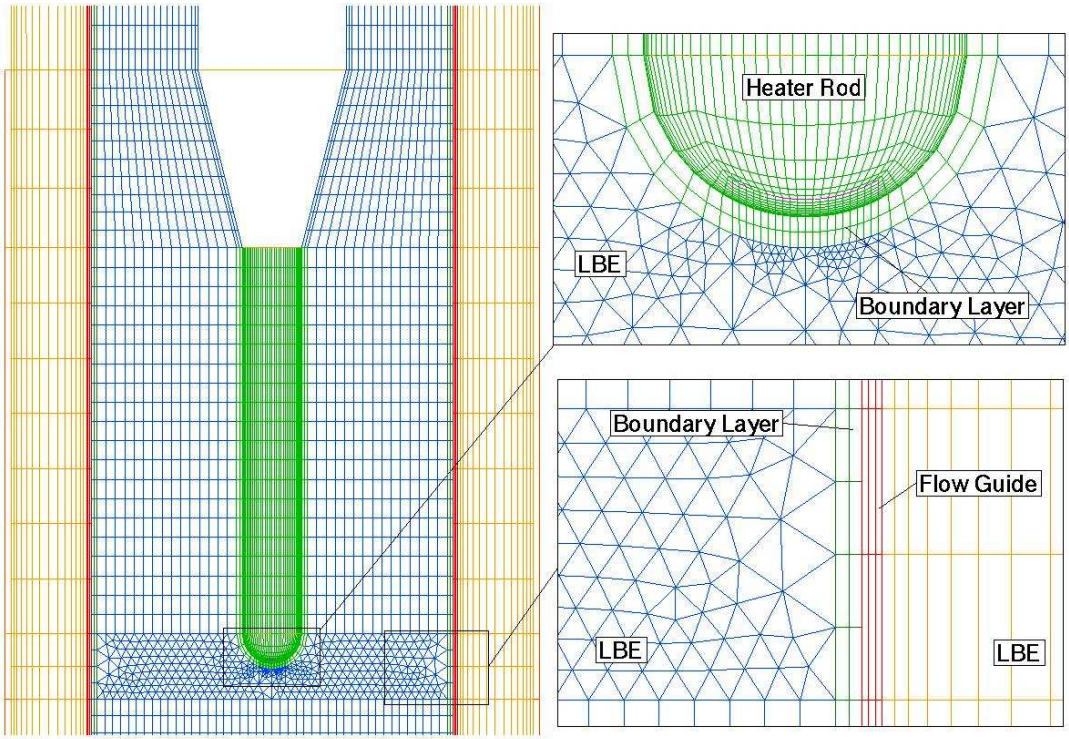

Figure 6 - Computational mesh: details of the instrumentation-rod region.

4.2 Spallation heat distribution

The spallation heat distribution reported in [13] was applied as a volumetric heat source in the simulation. The resulting power distributions are illustrated in Figure 7 and Figure 8 for case M1.0 (with the beam footprint major axis parallel to the guide-tube slant), and in Figure 9 and Figure 10 for case M1.1 (with the beam footprint major axis normal to the guide-tube slant). The total heat release in the various parts of the target is listed in Table 3, referred to the full domain (namely twice the one actually released in the computational domain).

Quantity	**Case M1.0**	**Case M1.1**
Total spallation heat	714614 W	714578 W
Heat released in the Pb-Bi	701462 W	701470 W
Heat released in the window	6042 W	6040 W
Heat released in the hull	574 W	574 W
Heat released in the flow-guide	6438 W	6494 W

Table 3 - Spallation heat deposit in the target (referred to the full domain) for cases M1.0 and M1.1.

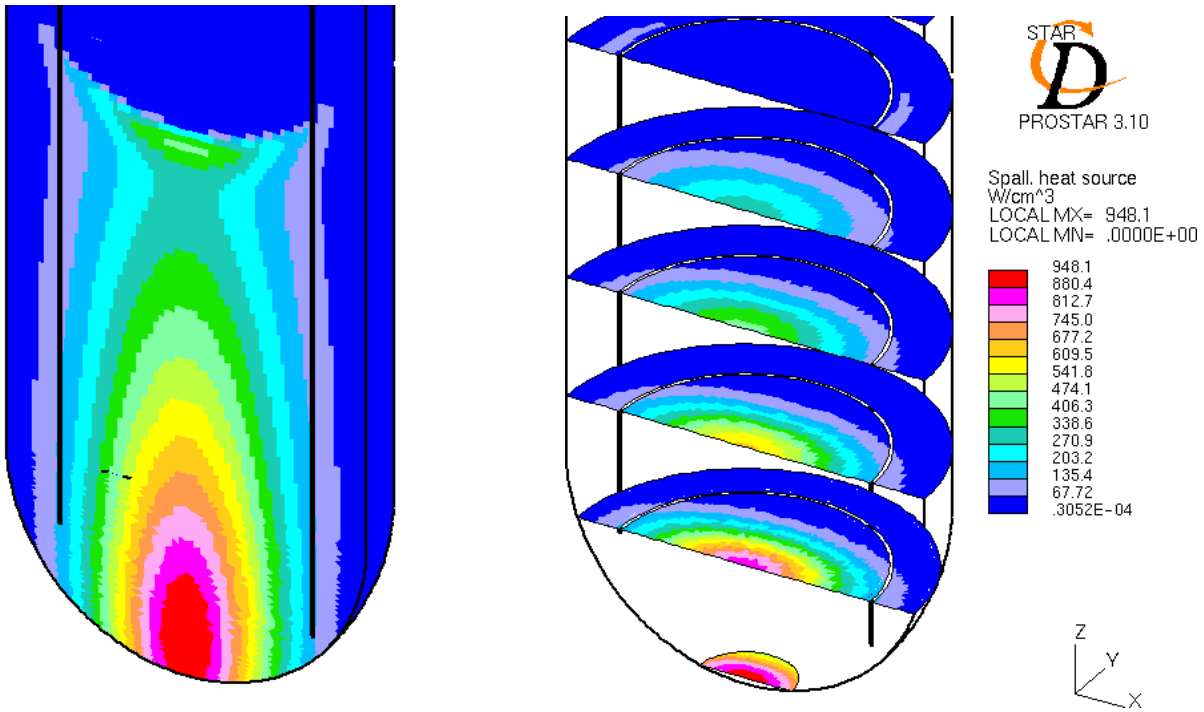

Figure 7 - Case M1.0: spallation heat distribution in the Pb-Bi.

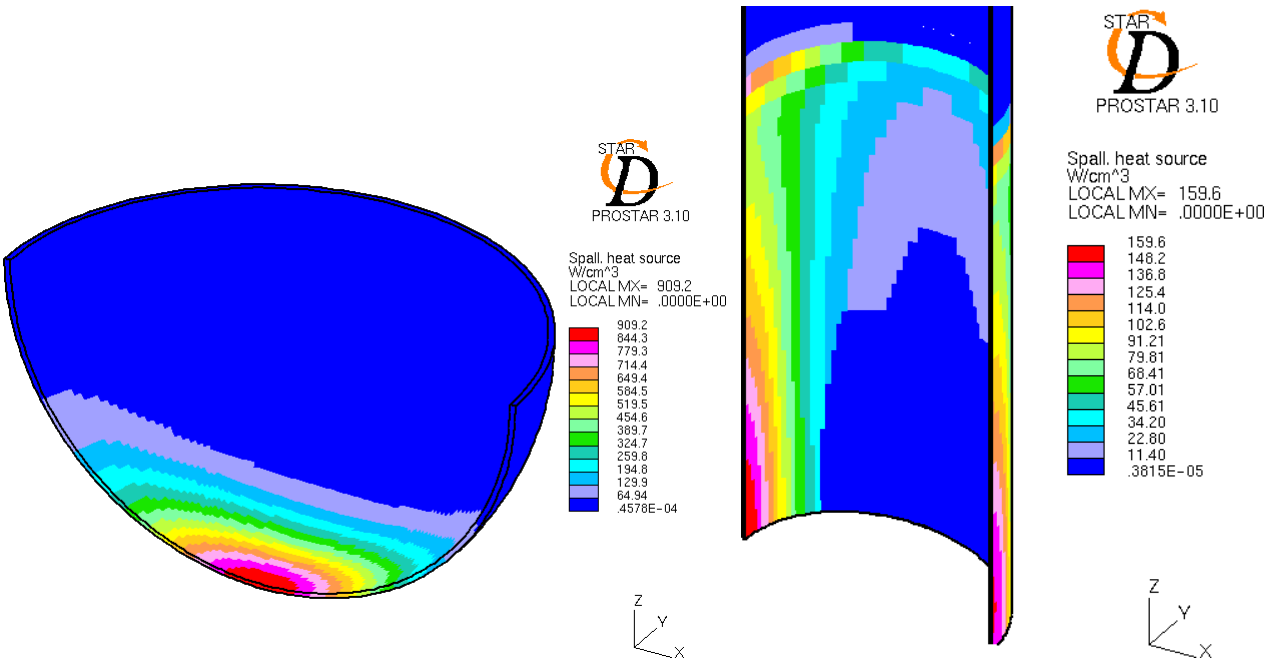

Figure 8 - Case M1.0: spallation heat-source distribution in the window (left) and in the guide tube (right).

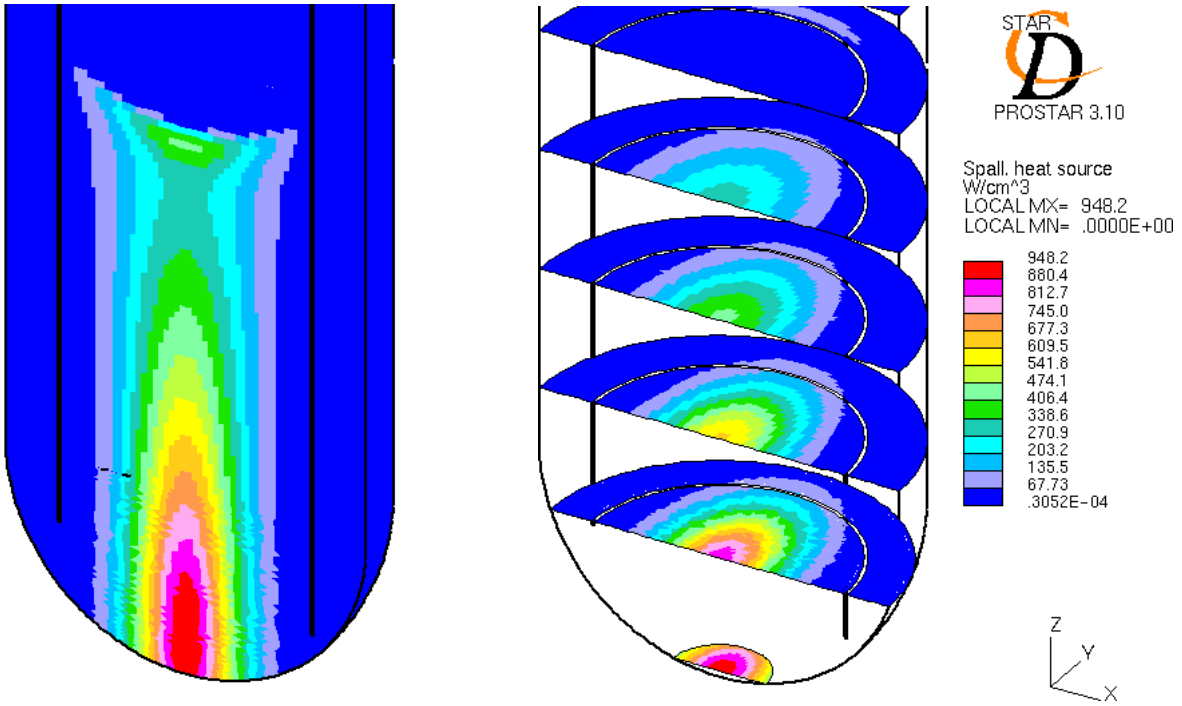

Figure 9 - Case M1.1: spallation heat distribution in the Pb-Bi.

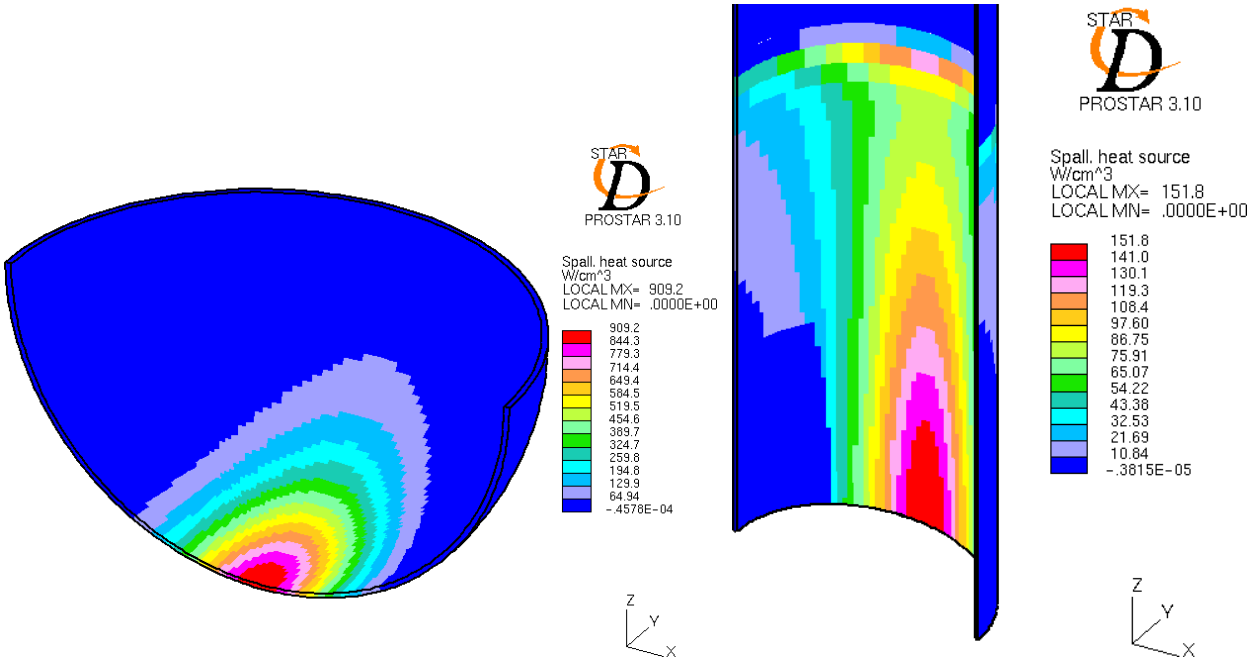

Figure 10 - Case M1.1: spallation heat-source distribution in the window (left) and in the guide tube (right).

4.3 Numerical schemes

Steady-state calculations were performed using the SIMPLE integration algorithm [12]. The following convection schemes were used:

- momentum equations: MARS;
- enthalpy equation: MARS;
- turbulence equations: MARS.

4.4 Turbulence modelling

A Chen k-ε model [12] was used for all the test cases performed. Either Wall-Functions or Two-Layer models [12] were used for the near-wall treatment, depending on the part of the domain considered (see Sec. 4.5.2).

4.4.1 Wall Functions

Star-CD Wall-Functions have been modified through user programming, in order to take into account the effect of the low Prandtl number of the Pb-Bi [14]. In particular, a dynamic switching from linear to logarithmic thermal boundary layer y_T^+ has been implemented as the larger root of the implicit equation [15]

$$\frac{Pr_t}{\kappa}\log(E_T\, y_T^+) = Pr\, y_T^+ \tag{1}$$

where κ=0.42, Pr_t = 0.9 and E_T is deduced from the following formula [15]

$$E_T = \exp\left\{9\kappa\left[\left(\frac{Pr}{Pr_t}\right)^{0.75} - 1\right]\left[1 + 0.28\exp\left(-0.007\frac{Pr}{Pr_t}\right)\right]\right\} \tag{2}$$

The resulting value of y_T^+ depends on the value of the molecular Prandtl number, which depends on temperature according to Table 1. As a result, y_T^+ grows with temperature. At the minimum temperature in the domain, namely the inlet temperature (230 °C), its value is about 235, and it grows up to about 500 at 400 °C. Therefore, being the maximum value y^+ in the domain where Wall Functions are applied about 150 (see Figure 11), the linear law (pure conduction) is always considered for thermal wall functions.

4.4.2 Turbulent Prandtl number

In two-equation turbulence models turbulent heat fluxes are modelled using a gradient-diffusion approach, where the turbulent heat diffusion coefficient α_t is set proportional to the turbulent cinematic viscosity ν_t through the turbulent Prandtl number

$$\alpha_t = \nu_t / Pr_t$$

The turbulent Prandtl number is usually considered constant and set to a standard value of 0.9. However, this approach could be unsuitable for liquid-metal flows, due to their very low molecular Prandtl number [16] [7].

In order to estimate the influence of the low Pr on the turbulent heat exchange, the following expression for Pr_t as a function of Pr and the turbulent Reynolds number Re_t has been deduced from [17]:

$$\mathrm{Pr}_t = c_1 + \frac{c_2}{\mathrm{Pr}\,\mathrm{Re}_t} \tag{3}$$

where $c_1 = 0.9$, $c_2 = 0.0899$ and

$$\mathrm{Re}_t = c_\mu^{-0.25}\,\frac{\nu_t}{\nu}.$$

Eq. (3) has been implemented in the CFD model and the results compared with the standard case with $\mathrm{Pr}_t = 0.9$ (see Sec. 6 and Sec. 7).

4.5 Boundary conditions

Inlet, outlet and symmetry boundary conditions were applied as illustrated in Figure 2. Conductive-wall boundary conditions were applied on all fluid-solid interfaces. All external walls were considered adiabatic, as well as the instrumentation-rod wall.

4.5.1 Inlet/Outlet

A uniform inlet velocity profile was considered with a velocity magnitude and a temperature as reported in Table 2. Inlet-flow turbulence characteristics should not have any influence on the flow characteristics in the lower part of the target, due to the considerable length of the down-coming duct. However, they can have some influence on the heat exchange across the guide tube in the upper part of the target. Lacking any precise information, a turbulence intensity of 0.2 and a turbulence length scale of 2 mm were assumed for the inlet flow.

A mass-flow preserving boundary condition [12] was applied on the flow outlet.

4.5.2 Fluid-solid interfaces

All fluid solid interfaces were considered as conductive walls with zero thermal resistance. Wall-Functions were used in the region where the flow was supposed to be more uniform (as in the downcomer) and on adiabatic walls (like the instrumentation rod). Figure 11 shows the typical distribution of y^+ on the walls where Wall Functions were applied.

A Norris & Reynolds Two-Layer algorithm [12] was used in critical parts like the window surface and the guide-tube in the spallation region, as illustrated in Figure 12.

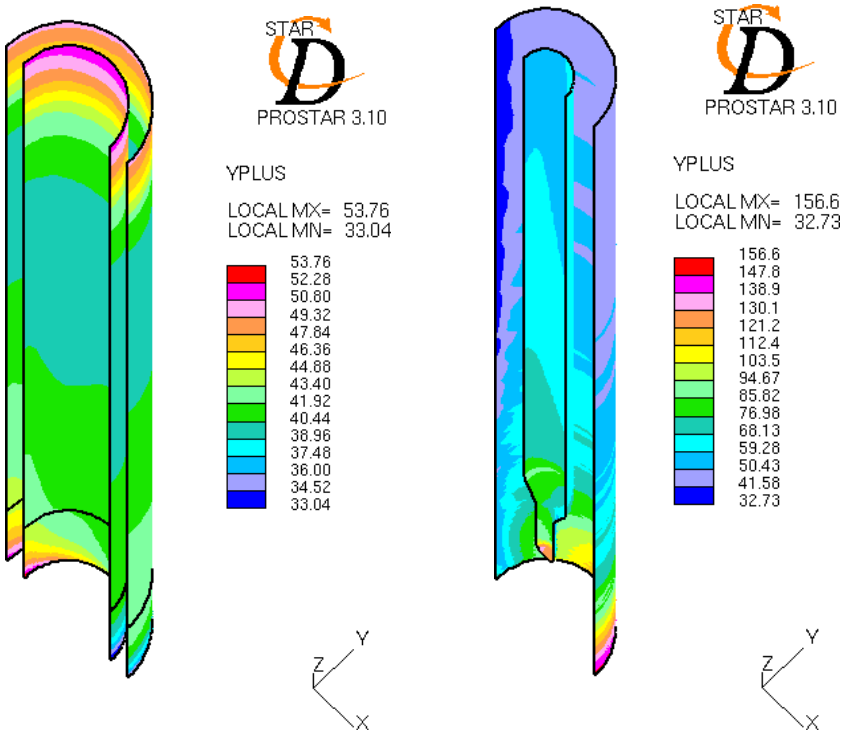

Figure 11 - Typical distribution of y^+ in the downcomer (left) and riser (right) walls.

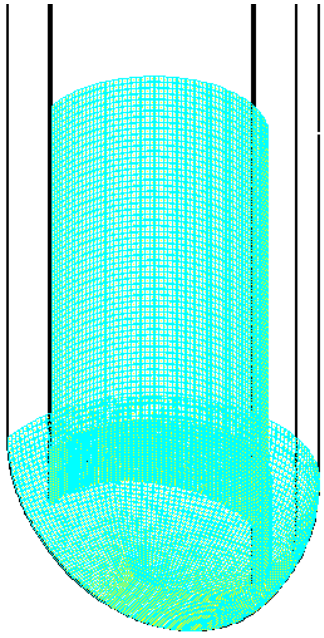

Figure 12 - Wall boundary conditions treated with the Two-Layer algorithm.

5 List of Test Cases

The test cases performed are listed in (Table 4). Both case M1.0 and M1.1 have been simulated with $Pr_t = 0.9$ and with Pr_t given by Eq. (3).

Case	Beam footprint major axis orientation	Turbulent Prandtl number
M1.0-*a*	parallel to the guide-tube slant	0.9
M1.0-*b*	parallel to the guide-tube slant	$0.9 + 0.0899/Pr/Re_t$
M1.1-*a*	normal to the guide-tube slant	0.9
M1.1-*b*	normal to the guide-tube slant	$0.9 + 0.0899/Pr/Re_t$

Table 4 - List of test cases.

6 Results for benchmark M1.0

6.1 Convergence

The convergence history for case M1.0 is illustrated in Figure 13. Residuals are normalised with the residual at the 10^{th} iteration and are reported in logarithmic scale. Graphs reported are valid for both cases *a* and *b*. Case *b* was run with a restart from the *a* solution at iteration 1800. The switching from constant to variable Prandtl number can be observed only in the solid-materials residuals.

Convergence is very good for all equations (below three or four orders of magnitude). Only in the case of the fluid enthalpy equation, residuals stay between two and three orders of magnitude (4×10^{-3}) lower then the 10^{th} residual. It is anyway an acceptable degree of convergence, having also checked that the solution was steady through monitoring of the maximum temperature in the flow.

6.2 Results for case *a* ($Pr_t = 0.9$)

The main flow characteristics are listed in Table 5, Table 6 and Table 7. The resulting velocity field in the lower part of the target is described in Figure 14 and Figure 15. The slanted guide-tube generates a highly vortical structure starting from the window surface, near the lower part of the slant, and diffusing along the riser in the spallation region. This vortex swirls and deforms the recirculation region generated behind the guide-tube by the flow reversing from the downcomer to the riser, whose dimension grows rotating around the guide tube. This is shown in Figure 15, where the velocity field is plotted on cutting planes at an angle α of 0^o, 45^o, 90^o and 135^o with respect to the x-z plane. In the plane at $\alpha=90^o$ (y-z plane) the swirling give rise to two recirculation regions: one near the guide tube and one near the symmetry plane. The dimension of the recirculation regions in planes x-z and y-z can be estimated from Figure 16, where the w velocity component is plotted (see Table 7). The swirling pattern is also put in evidence in the same figure through plotting the u-v vector field in different z planes, while the zone of the window where the vortex is generated can be seen in Figure 17. The stagnation point on the window is localised in the vortex centre (Table 7). The maximum flow velocity is 1.347 m/s and is localised in the vortex near the window (Table 6).

The resulting temperature fields in the Pb-Bi and in the window are shown in Figure 18 and Figure 20. A maximum temperature of 521 °C and 487 °C is reached in the external and internal side of the

window respectively (Table 6). The maximum flow temperature (486 °C) is reached nearby the window centre, but this peak, mainly generated by the heat transfer from the window, is quickly smoothed down by the vortical flow. Another hot structure is generated in the low-velocity recirculation region behind the guide tube by the spallation heat-source, and is convected by the swirling rising flow.

The effects of this hot plume on the flow along the riser, where buoyancy effects become more important due to the lower velocity, are shown in Figure 21, where the outlet velocity and temperature fields are plotted. It can be noticed that a faster stream is generated by the hot plume.

A relevant heat exchange takes place across the flow-guide from the rising flow to the down-coming flow (about 30 % of the total spallation heat, see Table 5), which increase the down-coming flow temperature of about 34 °C before reaching the spallation region.

The inlet-outlet total-pressure difference is about 1800 Pa (Table 5). In order to estimate the dissipation losses, the buoyancy pumping pressure should be added. This has been estimated as

$$\Delta p_b = g\,\rho\,\beta\,\Delta T\,H \cong 3300 \text{ Pa}$$

where g=9.81 m/s is the gravity acceleration, β is the Pb-Bi thermal expansion coefficient ($\rho\beta=\partial\rho/\partial T$=1.37 Kg/m^3/ °C, see Table 1), ΔT is the mean inlet-outlet temperature difference (~122 °C) and H is the target height (~2 m).

6.3 Results for case *b* ($Pr_t = f(Re_t, Pr)$)

Figure 22 shows the distribution of turbulence kinetic energy and turbulent viscosity in the lower part of the target and Figure 23 shows the corresponding fields of Re_t and Pr_t, calculated with Eq. (3). The variation of Pr_t with respect to the standard value of 0.9 remains within 5 % in the bulk flow (it obviously grows towards infinity while approaching walls). The variation is more evident in the near-window regions out of the vortex, in the downcomer and in the upper part of the riser. The corresponding variation of the turbulent thermal diffusion coefficient cannot be appreciated from the plot in Figure 24.

Figure 25 shows the profiles of Re_t and Pr_t along the z-axis starting from the window centre. It can be seen that Pr_t starts varying significantly at a distance from the wall of about 0.6 mm, corresponding to $y^+ \sim 20$. At that distance, the turbulent viscosity is rapidly decreasing, so that the effect on the thermal diffusion coefficient is minor, as can be seen in Figure 26.

The final effect on the flow field is a slight worsening of the heat exchange at walls. The heat exchanged across the flow guide is reduced of about 3% (Table 5), causing a slight reduction of the bulk flow temperature in the spallation region (Figure 19). However, the worse window cooling causes a maximum temperature increase of about 3 °C in both the window and the Pb-Bi (Table 6).

The effect of the worsen heat exchange on the velocity field is negligible in the spallation region, where buoyancy effects are not relevant, and is minor in the rest of the flow field, as it can be deduced comparing the velocity data reported in Table 6.

6.4 Tables and figures for case M1.0

Quantity	**Case *a***	**Case *b***
Outlet mean velocity	0.404 m/s	0.404 m/s
Outlet mean temperature	352 °C	352 °C
Inlet-outlet enthalpy flux difference	714872 W	712350
Total pressure loss (estimated buoyancy pumping pressure ~3300 Pa)	1762 Pa	1774 Pa
Area-averaged temperature of the external side of the guide tube	305 °C	305 °C
Area-averaged temperature of the internal side of the guide tube	325 °C	324 °C
Heat transferred from the guide tube to the down-coming flow	202634 W	197168 W

Table 5 - Case M1.0: global results (extensive quantities are referred to the full domain).

Quantity	**Value (position x,y,z [mm])** **Case *a***	**Value (position x,y,z [mm])** **Case *b***
Maximum Pb-Bi velocity	1.347 m/s (36, 36, 17)	1.347 m/s (36, 36, 17)
Maximum Pb-Bi temperature	486 °C (5, 1, 0)	489 °C (3, 1, 0)
Maximum outlet velocity	0.462 m/s (24, 31, 2150)	0.461 m/s (24, 31, 2150)
Maximum outlet temperature	375 °C (23, 11, 2150)	374 °C (23, 11, 2150)
Maximum window external surface temperature	521 °C (3, 2, -1)	524 °C (3, 2, -1)
Maximum window internal surface temperature	487 °C (5, 1, 0)	490 °C (3, 1, 0)
Maximum flow-guide temperature	376 °C (-61, 1, 70)	369 °C (-41, 46, 283)
Maximum instrumentation rod temperature	381 °C (10, 0, 625)	375 °C (-61, 1, 70)

Table 6 - Case M1.0: maximum temperatures and velocities with their location for cases *a* and *b*.

Position of the stagnation point on the window (x, y, z) [mm]	37, 32, 15
Minimum and maximum y^+ value on the window	0.3 - 7.1
Height of first recirculation region in the x=0 plane (beside the guide tube)	40 mm
Height of second recirculation region in the x=0 plane (beside the symmetry plane)	60 mm
Height of recirculation region in the y=0 plane (beside the guide tube)	130 mm

Table 7 - Case M1.0: window stagnation point and y^+ and recirculation regions size. These data are valid both for case *a* and *b*.

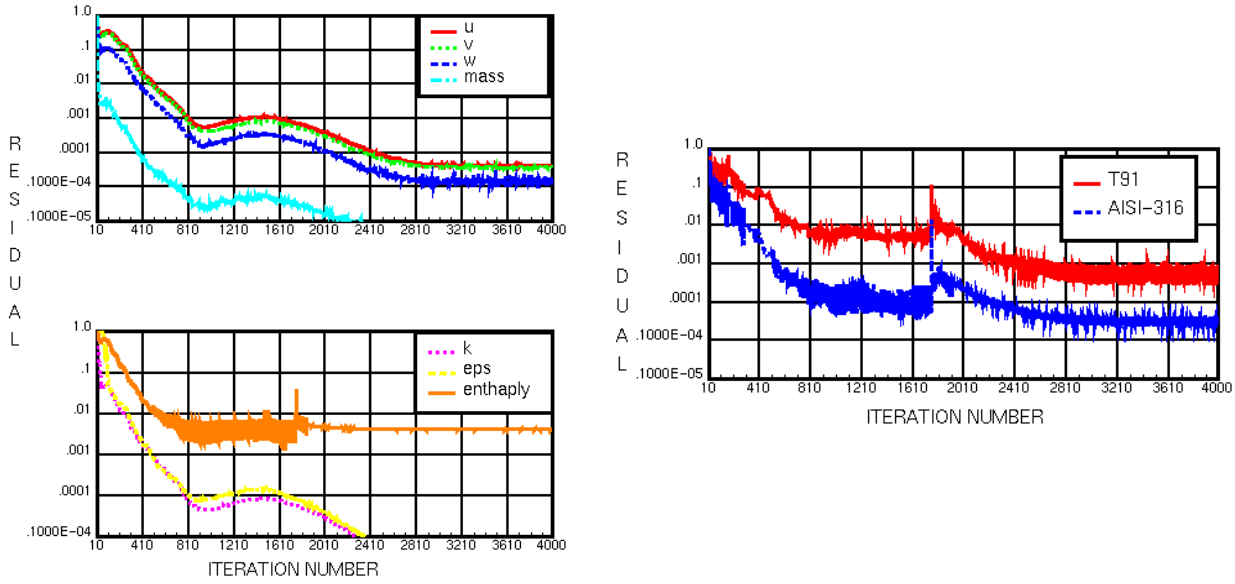

Figure 13 - Case M1.0: residuals history in the fluid (left) and in the solid materials.

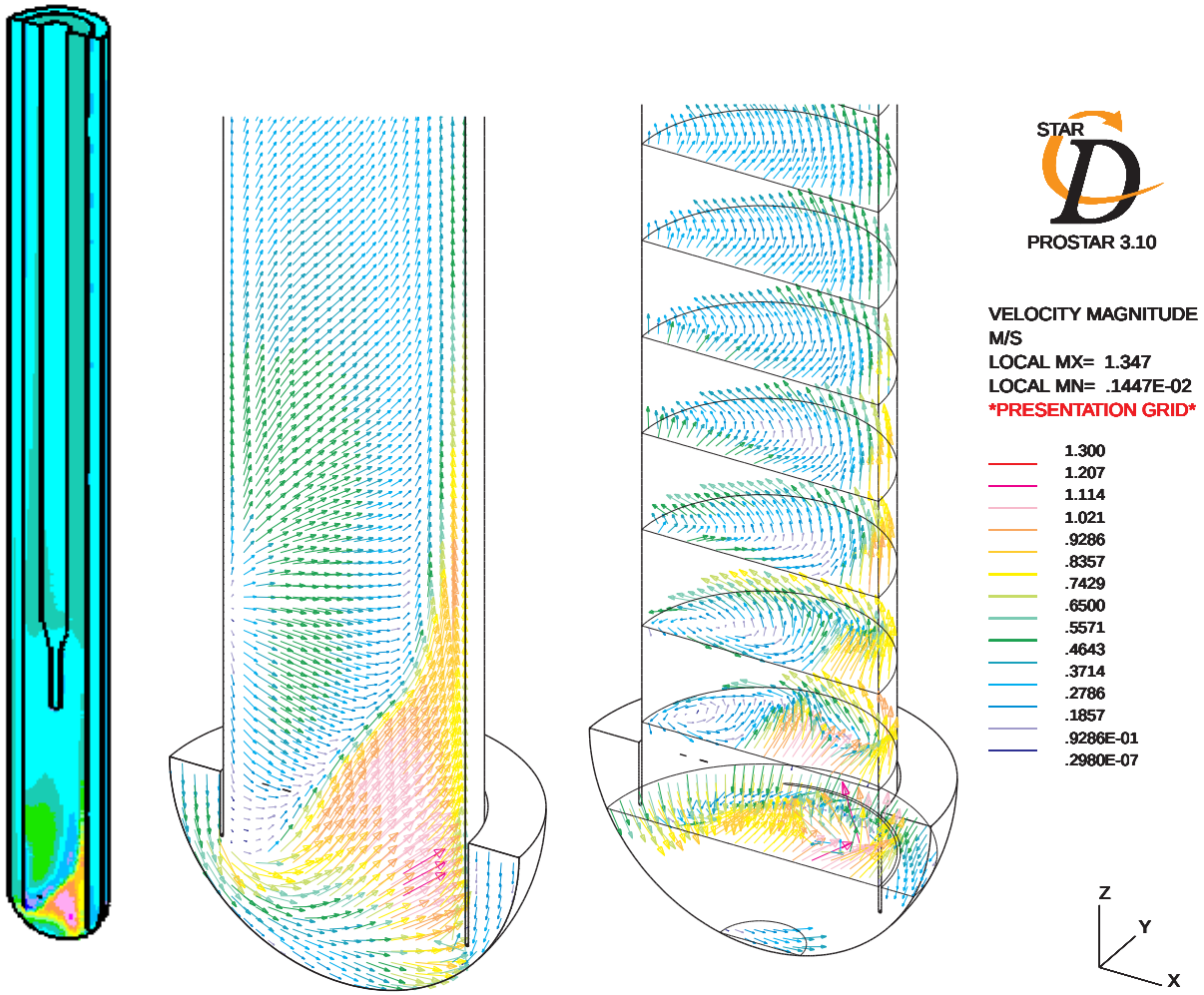

Figure 14 - Case M1.0-*a*: velocity magnitude in the whole target (left) and velocity-vector fields in the spallation region on plane y=0 (centre) and on various z planes (right).

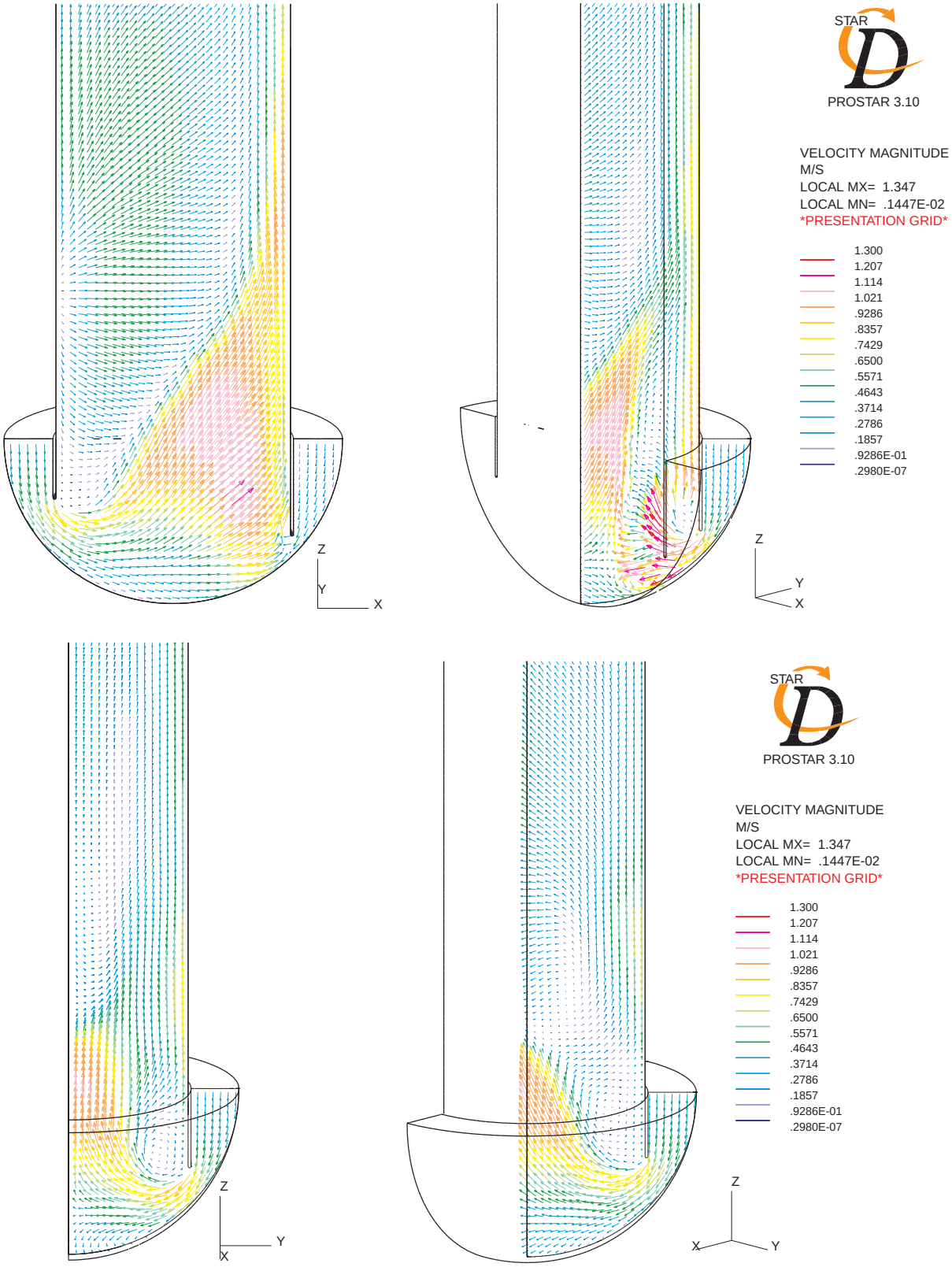

Figure 15 - Case M1.0-*a*: velocity-vector fields in the spallation region on planes at an angle of 0, 45, 90, 135 deg with respect to the x-z plane.

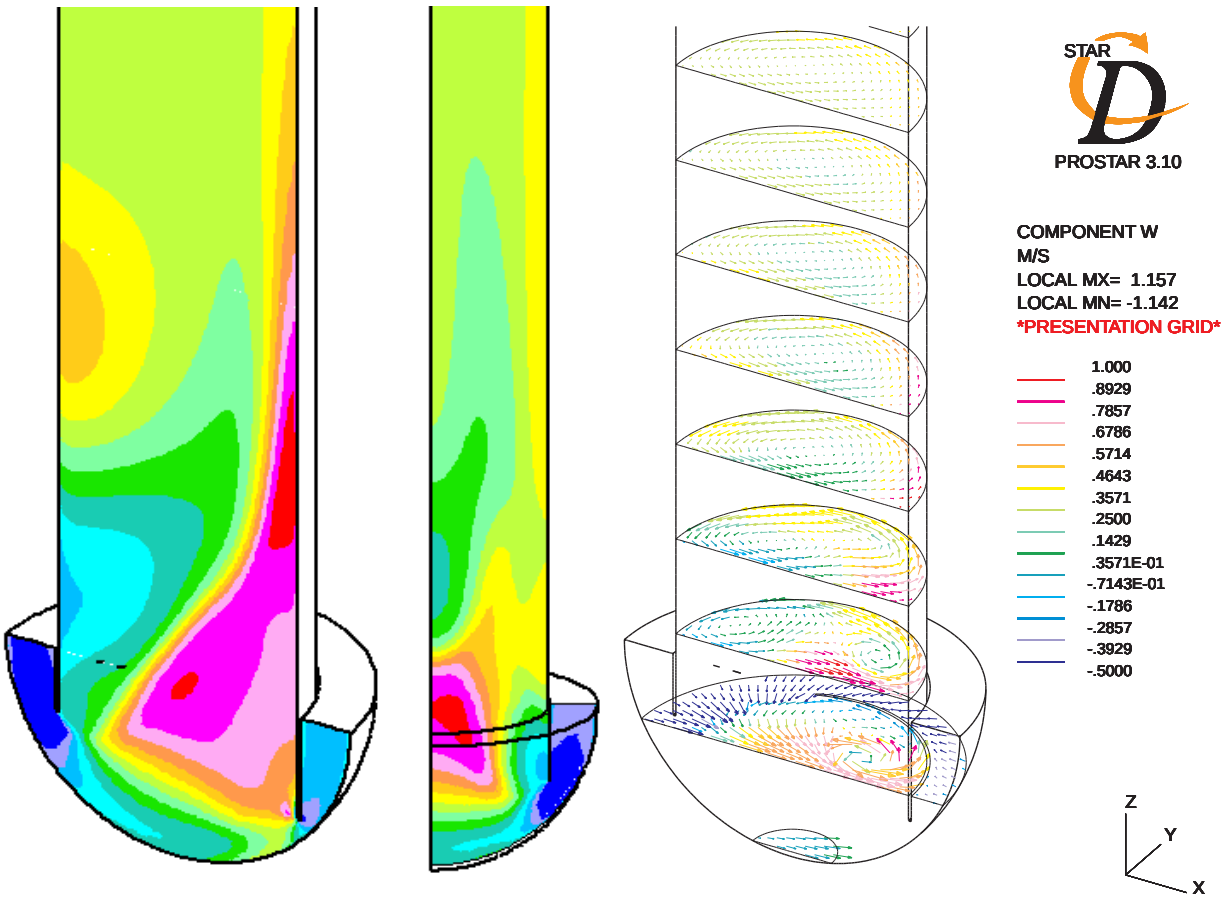

Figure 16 - Case M1.0-*a*: w velocity component in planes y=0 (left) and x=0 (centre) and uv vector field on different z planes (right).

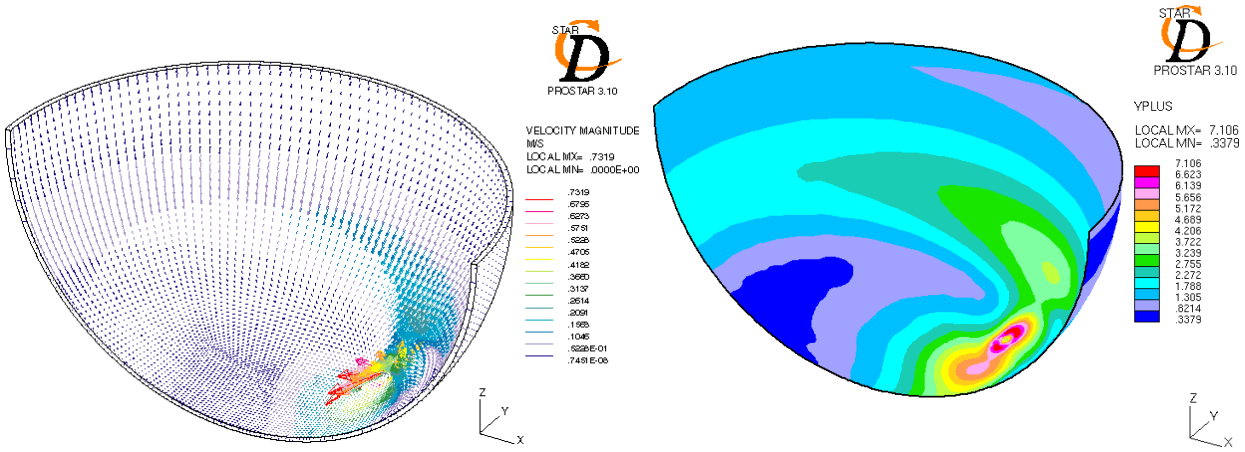

Figure 17 - Case M1.0-*a*: velocity-vector field (left) and y^+ distribution in the first layer of cells nearby the window (distance of the first near-wall cell 1.3×10^{-2} mm).

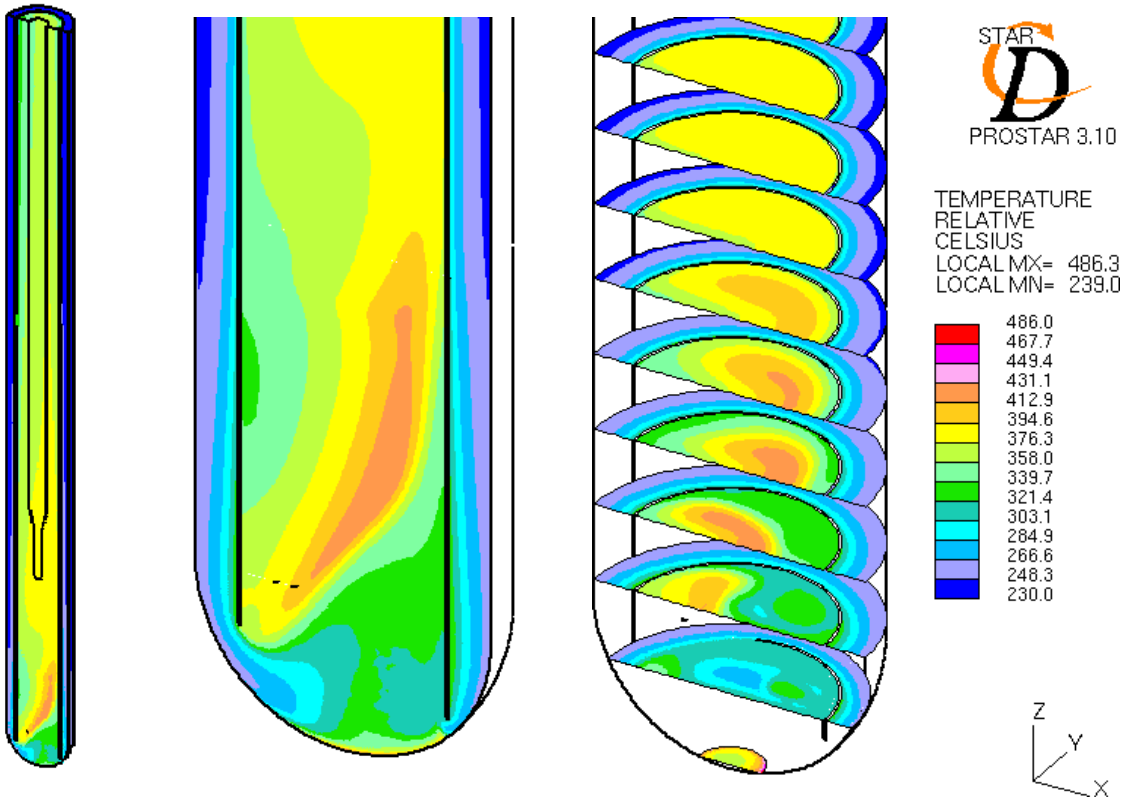

Figure 18 - Case M1.0-*a*: temperature field in the whole target (left) and in the spallation region on plane y=0 (centre) and on various z planes (right).

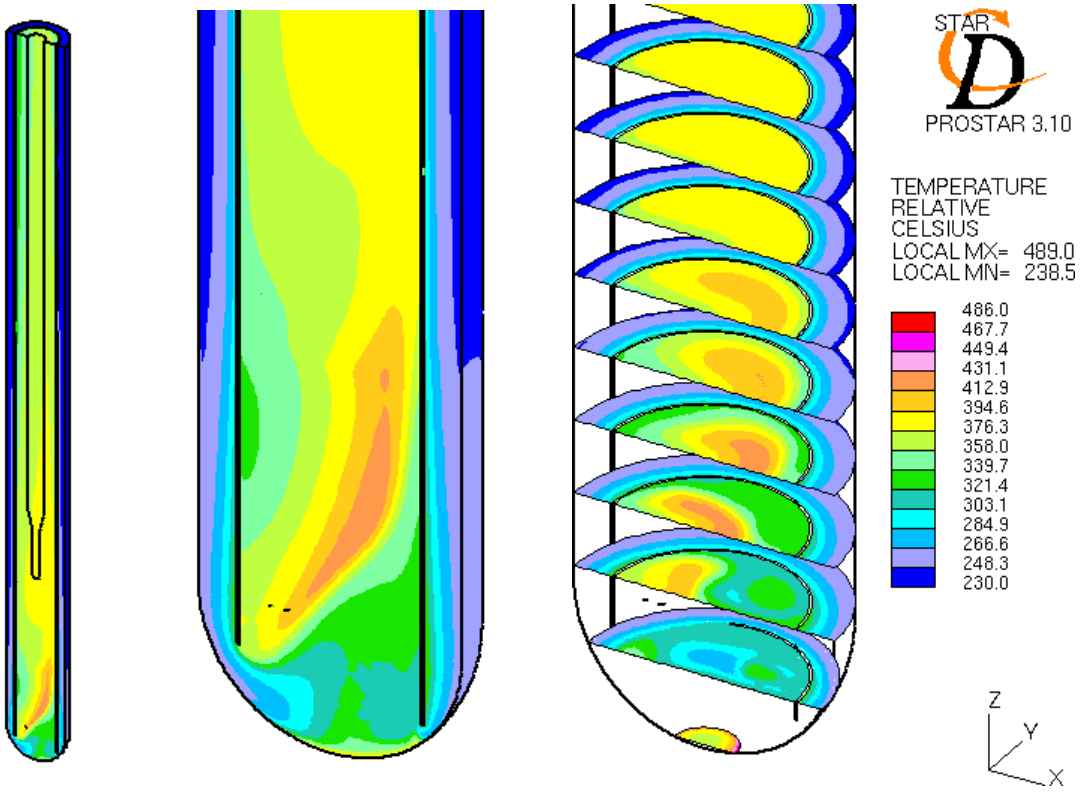

Figure 19 - Case M1.0-*b*: temperature field in the whole target (left) and in the spallation region on plane y=0 (centre) and on various z planes (right).

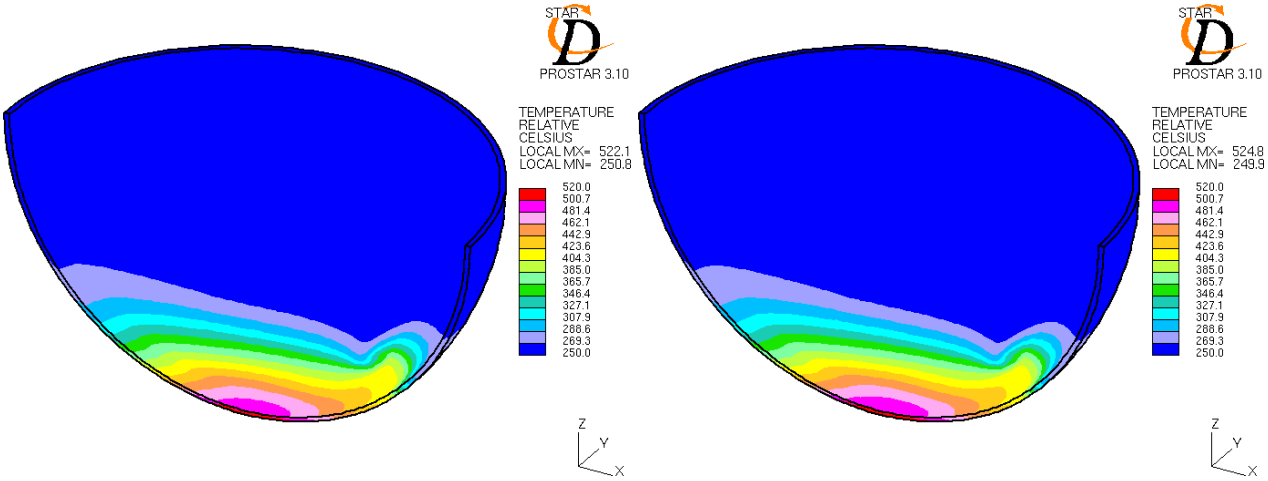

Figure 20 - Temperature field in the window for cases M1.0-*a* (left) and M1.0-*b* (right).

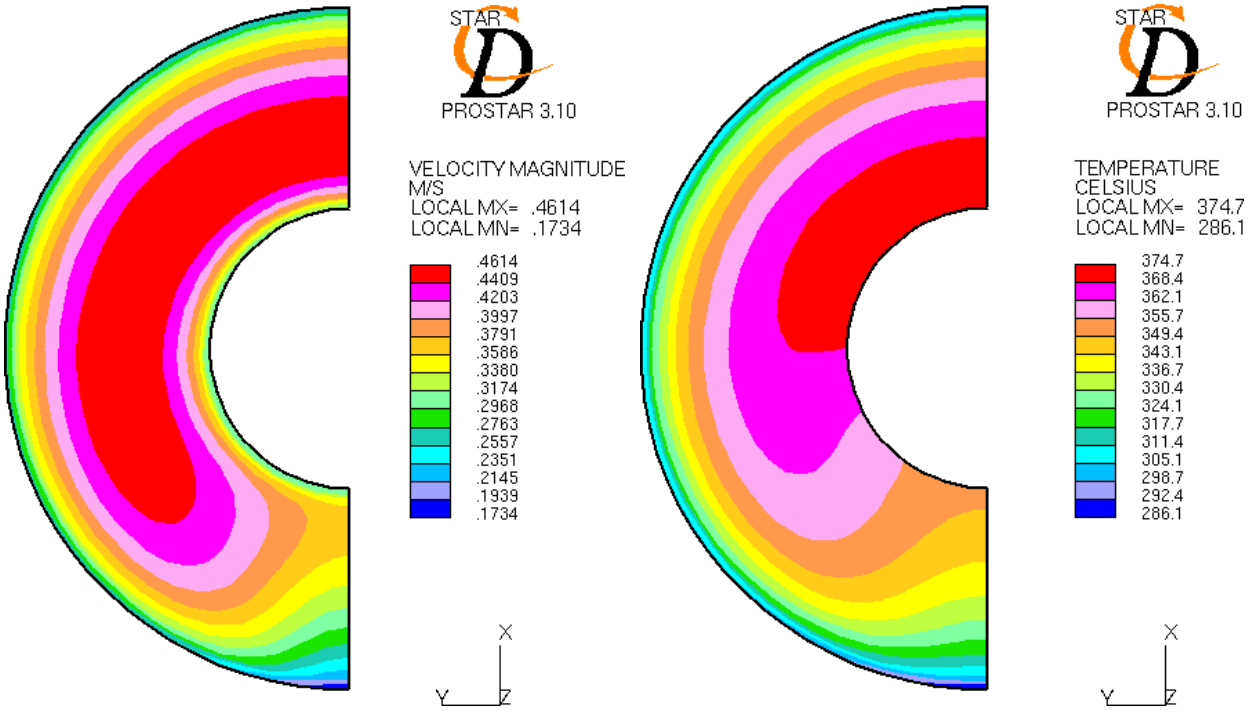

Figure 21 - Case M1.0-*a*: velocity magnitude (left) and temperature (right) fields in the outlet section.

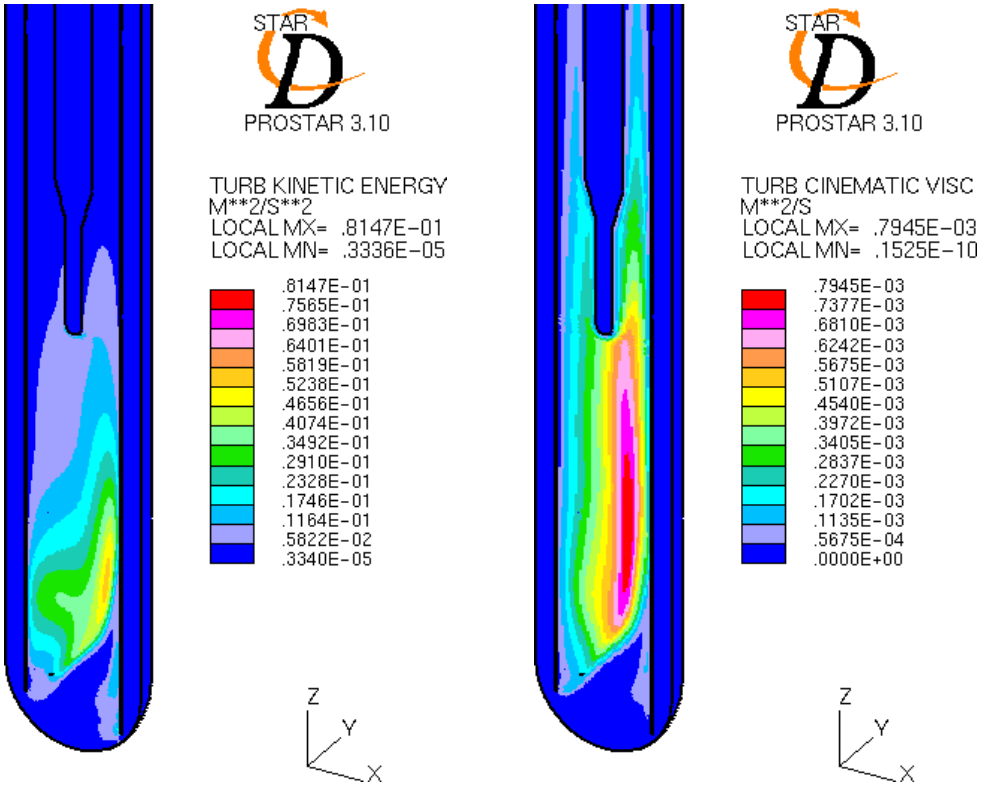

Figure 22 - Case M1.0-*b*: distribution of turbulent kinetic energy (left) and turbulent cinematic viscosity (right).

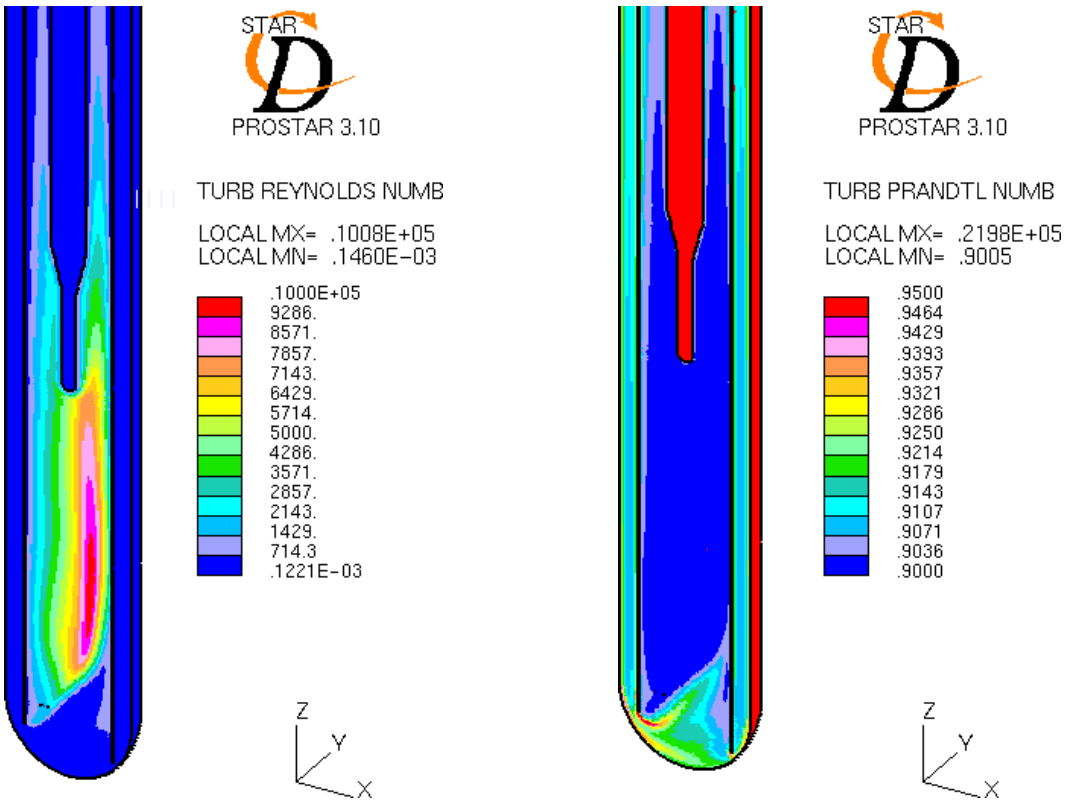

Figure 23 - Case M1.0-*b*: distribution of turbulent Reynolds number (left) and turbulent Prandtl number (right).

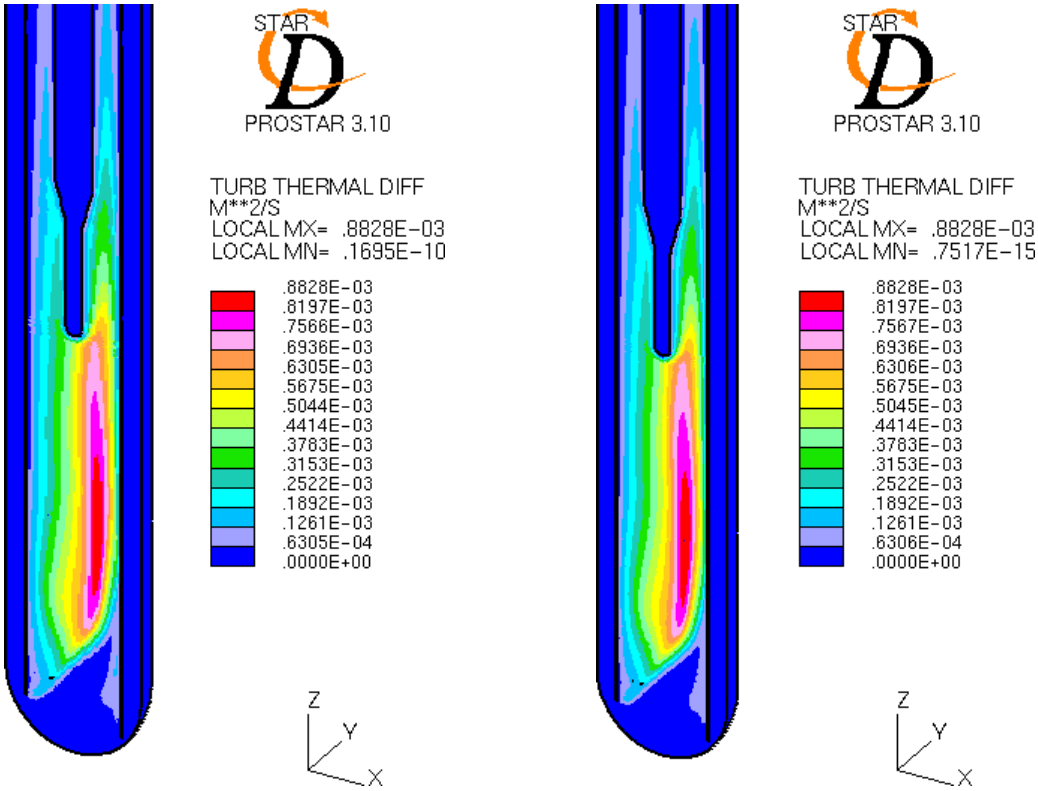

Figure 24 - Distribution of turbulent thermal diffusion coefficient for cases M1.0-*a* (left) and M1.0-*b* (right).

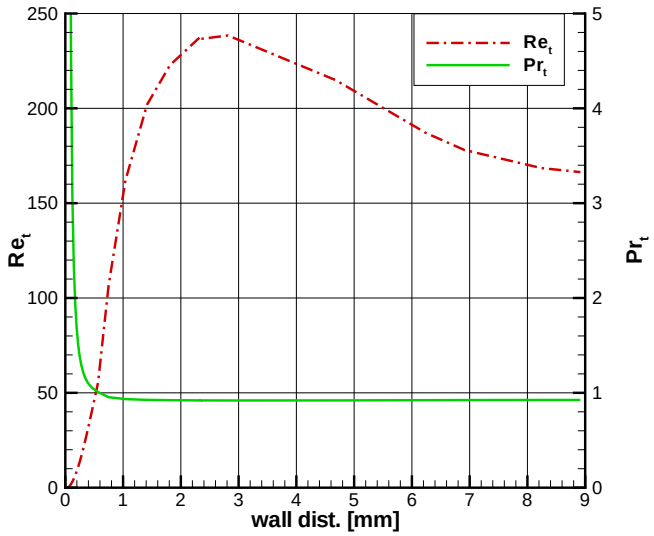

Figure 25 - Case M1.0-*b*: profiles of turbulent Reynolds and Prandtl numbers along the z axis starting from the window centre.

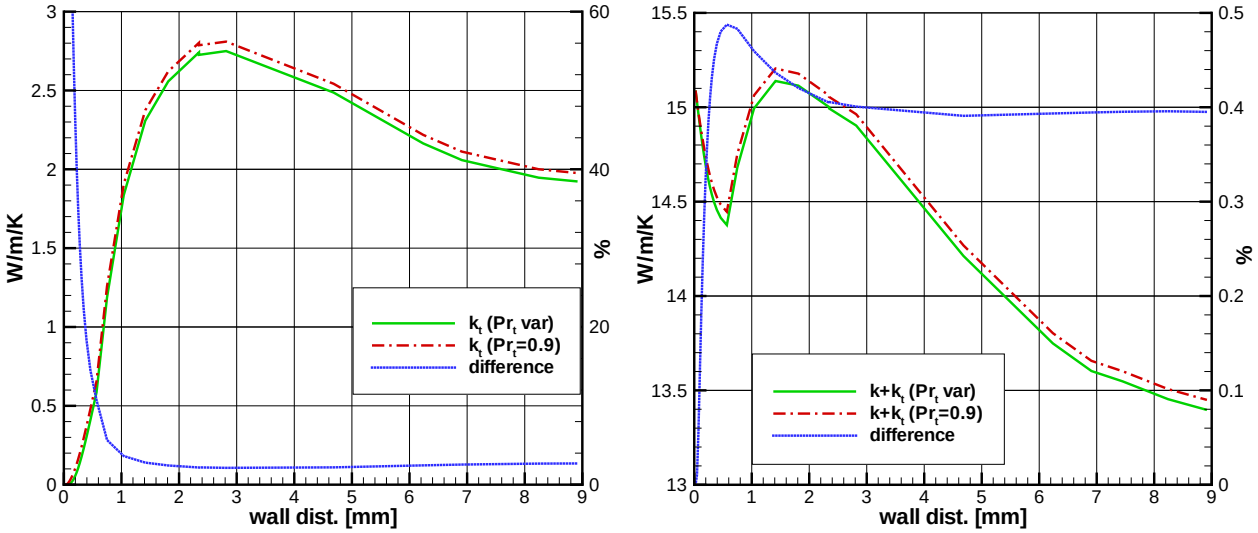

Figure 26 - Case M1.0: profiles of turbulent and total (molecular + turbulent) thermal conduction coefficient along the z-axis starting from the window centre: comparison between cases with constant (case *a*) and variable (case *b*) turbulent Prandtl number.

7 Results for case M1.1

7.1 Convergence

Almost the same convergence history as in case M1.0 was obtained (see Figure 13).

7.2 Results for case *a* ($Pr_t = 0.9$)

Being buoyancy effects of minor importance in the spallation region, the flow pattern is very similar to the one illustrated for case M1.0. This can be deduced comparing the velocity data reported in Table 6 and Table 9: the maximum flow velocities differ of about of 0.5 % and the outlet maximum velocities of about 1 %. The former are located almost in the same position, while a slightly different velocity distribution can be observed in the outlet section (see Figure 21 and Figure 30). Also, the position of the stagnation point on the window is the same, while the estimated dimensions of the recirculation regions are slightly different (Table 10)

The temperature field in the Pb-Bi and in the window are shown in Figure 27 and Figure 29. Being the beam major axis perpendicular to the flow main direction, the window-cooling flow undergoes a lower heating with respect to case M1.0. As a consequence, window temperatures are sensibly lower (about 70 ^{o}C) and the maximum temperature in the Pb-Bi is no more located near the window, but in the upper part of the spallation region (see Table 9 and Figure 27).

7.3 Results for case *b* ($Pr_t = f(Re_t, Pr)$)

As for case M1.0, the variable turbulent Prandtl number does not change the main flow characteristics. Also in this case, the lower heat exchange across the guide tube (Table 8) cause a lower temperature increase of the down-coming flow, and therefore slightly lower Pb-Bi bulk temperatures (Figure 28). Being the maximum Pb-Bi temperature located in the bulk flow, it results to be lower in case *b* than in case *a* (about 1 ^{o}C, see Table 9). This effect, combined with the reduced heat exchange with the window, results in a window temperature increase of about 2 ^{o}C with respect to case *a* (Table 9).

7.4 Tables and figures for case M1.1

Quantity	**Case *a***	**Case *b***
Outlet mean velocity	0.404 m/s	0.404 m/s
Outlet mean temperature	352 °C	352 °C
Inlet-outlet enthalpy flux difference	714584 W	712472 W
Total pressure loss (estimated buoyancy pumping pressure ~3300 Pa)	1800 Pa	1780 Pa
Area-averaged temperature of the external side of the guide tube	304 °C	304 °C
Area-averaged temperature of the internal side of the guide tube	324 °C	323 °C
Heat transferred from the guide tube to the down-coming flow	200252 W	194980 W

Table 8 - Case M1.1: global results (extensive quantities are referred to the full domain)

Quantity	**Value (position x,y,z [mm])** **Case *a***	**Value (position x,y,z [mm])** **Case *b***
Maximum Pb-Bi velocity	1.354 m/s (34, 35, 16)	1.354 m/s (34, 35, 16)
Maximum Pb-Bi temperature	425 °C (1, 31, 265)	423 °C (1, 28, 265)
Maximum outlet velocity	0.468 m/s (37,1, 2150)	0.467 m/s (37,1, 2150)
Maximum outlet temperature	376 °C (25, 1, 2150)	375 °C (25, 1, 2150)
Maximum window external surface temperature	447 °C (6, 2, -1)	449 °C (6, 2, -1)
Maximum window internal surface temperature	414 °C (8, 1, 0)	416 °C (8, 1, 0)
Maximum flow-guide temperature	370 °C (-41, 46, 283)	369 °C (-41, 46, 283)
Maximum instrumentation rod temperature	385 °C (10, 0, 586)	384 °C (10, 0, 586)

Table 9 - Case M1.1: maximum temperatures and velocities with their location for cases *a* and *b*.

Position of the stagnation point on the window (x, y, z) [mm]	37, 32, 15
Height of first recirculation region in the x=0 plane (beside the guide tube)	40 mm
Height of second recirculation region in the x=0 plane (beside the symmetry plane)	55 mm
Height of recirculation region in the y=0 plane (beside the guide tube)	150 mm

Table 10 - Case M1.1: window stagnation point and recirculation regions.

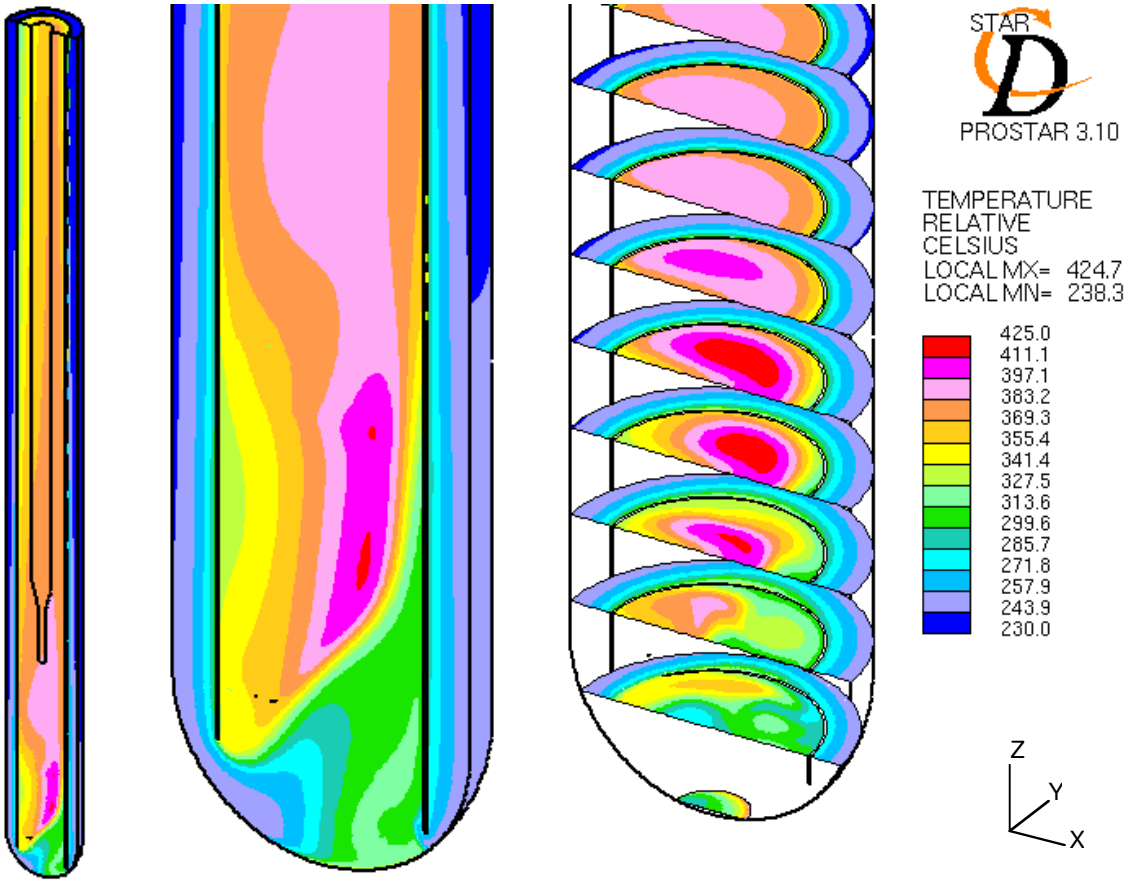

Figure 27 - Case M1.1-*a*: temperature field in the whole target (left) and in the spallation region on plane y=0 (centre) and on various z planes (right).

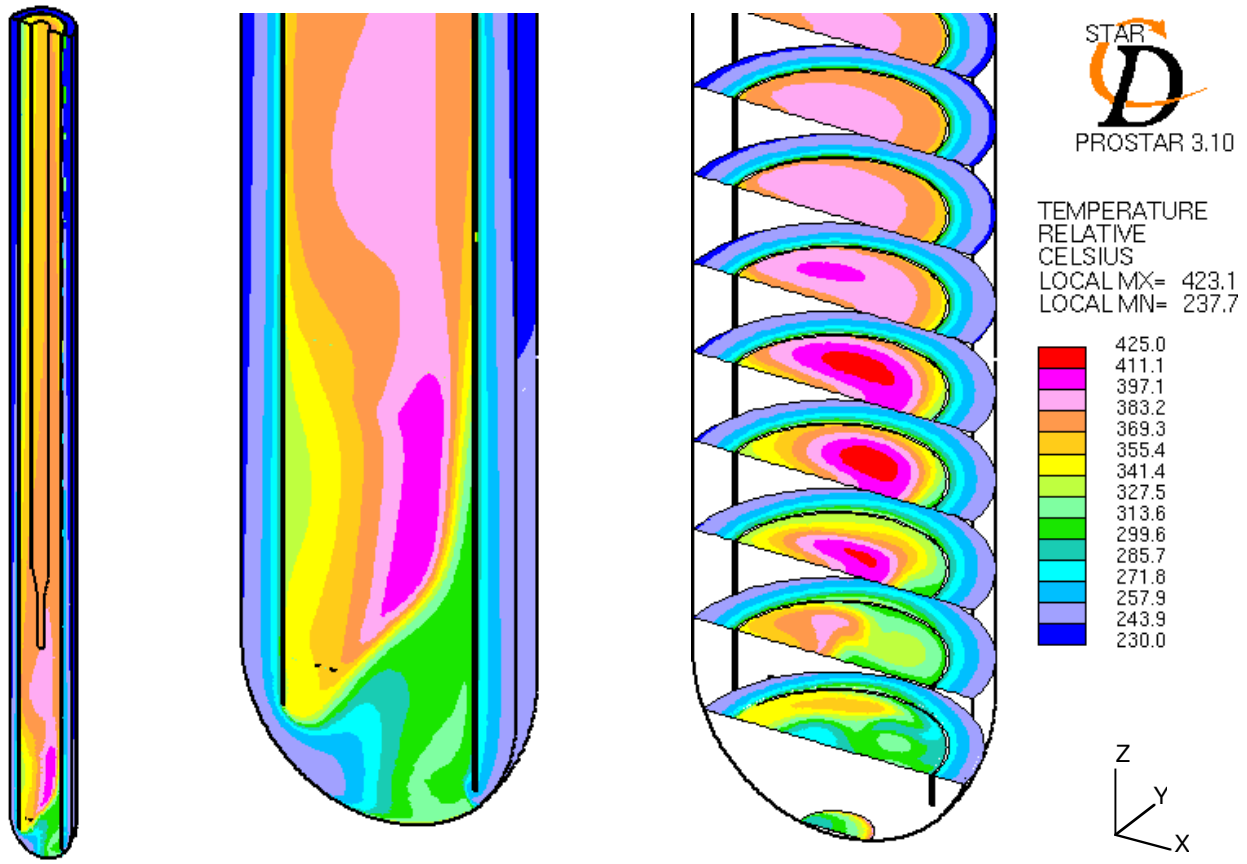

Figure 28 - Case M1.1-*b*: temperature field in the whole target (left) and in the spallation region on plane y=0 (centre) and on various z planes (right).

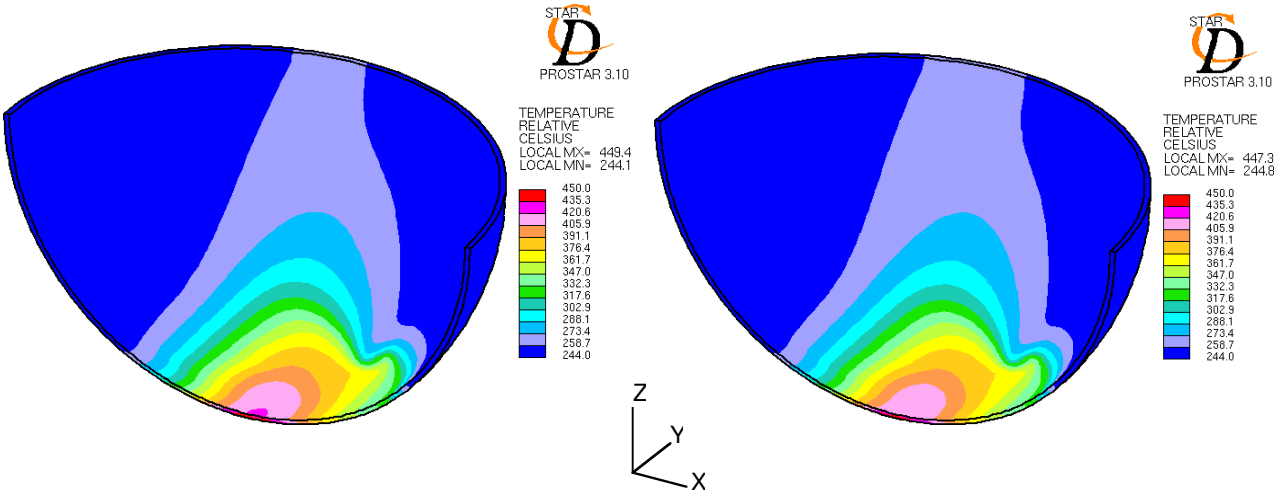

Figure 29 - Temperature field in the window for cases M1.1-*a* (left) and M1.1-*b* (right).

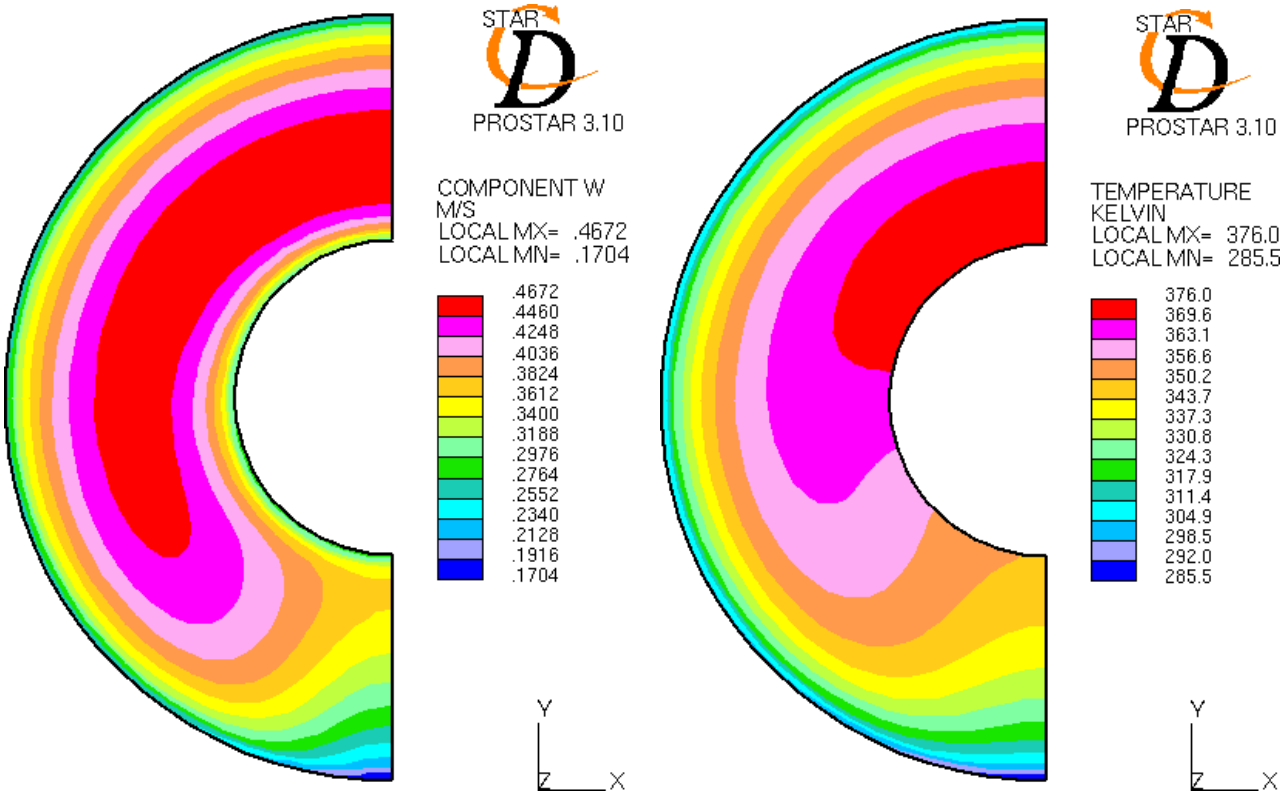

Figure 30 - Case M1.1-*a*: velocity magnitude (left) and temperature (right) fields in the outlet section.

8 Conclusions

Benchmark calculations M1.0 and M1.1 on the MEGAPIE target geometry with slanted guide tube have been performed using Star-CD. A Chen k-ε model was used, joined with both Two-Layer and Wall Functions, modified for liquid metals, for the near-wall turbulence modelling. An expression for the turbulent Prandtl number as a function of Pr and Re_t was implemented, and the results compared with the standard case Pr_t=0.9.

Results show a very complex flow pattern in the spallation region, with 3D vortex structures being generated in the reversing region and dragged along the rising duct.

In case M1.0 with Pr_t = 0.9, results show maximum window temperatures of 521 °C and 487 °C in the external and internal side respectively, with a maximum Pb-Bi temperature of 486 °C located nearby the window centre. The maximum flow velocity is 1.35 m/s. A significant heat exchange takes place across the 1.5 mm thick flow guide, causing a mean temperature increase along the down-comer of about 34 °C.

Due to the high Reynolds number of the flow, the effect of using a variable Pr_t is limited to near wall regions, where the heat exchange is slightly reduced. The combination of a lower heat exchange across the flow guide (resulting in a lower temperature increase of the Pb-Bi along the down-comer) and a worse window cooling yielded a maximum window temperature of 524°C, namely 3 °C more than in the case with Pr_t = 0.9.

Due to the limited effects of buoyancy in the spallation region, the flow pattern for case M1.1 is similar to the one obtained for case M1.0. In this case, the window-cooling flow undergoes a lower spallation heating, resulting in lower window temperatures. Maximum window temperatures of 447 °C and 414 °C were found using Pr_t = 0.9 with a maximum Pb-Bi temperature of 423 °C located in the central part of the spallation region. Using a variable Pr_t, window temperatures increased of about 2 °C while a 1 °C lower maximum Pb-Bi temperature was found.

9 References

[1] C. Rubbia et al., *Conceptual Design of a Fast Neutron Operated High Power Energy Amplifier*, CERN/AT/95-44 (ET), September 1995.

[2]ANSALDO, CRS4, ENEA, INFN, *Energy Amplifier Demonstration Facility Reference Configuration*, Summary Report, Ansaldo Nucleare EA B0.00 1 200, January 1999.

[3] European Joint Research Centre web site http://nucleartimes.jrc.nl.

[4] V. Bellucci, S. Buono, G. Fotia, L. Maciocco, V. Moreau, M. Mulas, G. Siddi, L. Sorrentino, *Requirements of the beam target of the Energy Amplifier prototype*, CRS4 Tech. Rep. 98/38, June 1998.

[5] ????

[6] http://www.crs4.it/Areas/ea/LSdesign/LSdesign.html,

http://www.fz-juelich.de/ess/CUR/ESS_Target_Concept.html,

http://www.sckcen.be/research/reactorsafety/fuel/myrrha/myrrha_home.html,

http://www.kalla.fzk.de/kalla/projects/megapieeu.html.

[7] Accompanying Measure on the Assessment of Computational Fluid Dynamics Codes for Heavy Liquid Metals - ASCHLIM, EU project FIS5-2001-0001.

[8] M. Salvatores, G.S. Bauer, G. Heusener, The MEGAPIE Initiative: Executive Outline and Status as per November 1999, MPO-1-GB-6/0_GB.

[9] T Dury, MEGAPIE Target Design Drawing of January 2001, PSI report, November 2th 2001.

[10] T. Dury, Minutes of the 9th X4-X6 Coordination Meeting, PSI, December 12th 2001.

[11]] IDEAS web page: http://www.scdc.com/ideas/index.shtml.

[12] Star-CD, Version 3.15 manual, Computational Dynamics, London, 2001.

[13] Trevor Dury, Best-estimate fit for MEGAPIE Heat Deposition Profile Data of 19.2.01, PSI internal note, November 30, 2001

[14] C. Aragonese, S. Buono, G. Fotia, L. Maciocco, V. Moreau, L. Sorrentino, *Benchmark calculations of Mercury flow experiments performed in Riga for the ESS target design*, CRS4 Tech. Rep. 99/21, November 1999.

[15] AEA Technology plc, *CFX-4.2 Solver*, December 1997.

[16] C. Aragonese, S. Buono, L. Maciocco, V. Moreau, L. Sorrentino, *CFD Simulation of a Heated Round Jet of Sodium in Forced Flow Regime (TEFLU Benchmark)*, CRS4 Tech. Rep. 00/86, July 2001.

[17] M. Jisha, H.B. Rieke, *Modelling assumptions for turbulent heat transfer*.